Title: Sensing whales, storms, ships and earthquakes using an Arctic fibre-optic cable

Authors: Martin Landrø[1]*, Léa Bouffaut[1], Hannah Joy Kriesell[1], John Robert Potter[1], Robin André Rørstadbotnen[1], Kittinat Taweesintananon[1], Ståle Emil Johansen[2], Jan Kristoffer Brenne[3], Aksel Haukanes[3], Olaf Schjelderup[4], Frode Storvik[4]

Affiliations:

[1]Department of Electronic Systems, Norwegian University of Science and Technology (NTNU); Trondheim, Norway.

[2]Department of Geoscience and Petroleum, Norwegian University of Science and Technology (NTNU); Trondheim, Norway.

[3]Alcatel Submarine Networks Norway AS; Tiller, Norway.

[4]Uninett AS; Trondheim, Norway.

*Corresponding author. Email: martin.landro@ntnu.no

Abstract: Our oceans are critical to the health of our planet and its inhabitants. Increasing pressures on our marine environment are triggering an urgent need for continuous and comprehensive monitoring of the oceans and stressors, including anthropogenic activity. Current ocean observational systems are expensive and have limited temporal and spatial coverage. However, there exists a dense network of Fibre-Optic (FO) telecommunication cables, covering

both deep ocean and coastal areas around the globe. FO cables have an untapped potential for advanced acoustic sensing that, with recent technological break-throughs, can now fill many gaps in quantitative ocean monitoring. Here we show for the first time that an advanced Distributed Acoustic Sensing (DAS) interrogator can be used to capture a broad range of acoustic phenomena with unprecedented signal-to-noise ratios and distances. We have detected, tracked, and identified whales, storms, ships, and earthquakes. We live-streamed 250 TB of DAS data from Svalbard to southern Norway via Uninett's research network over 44 days; a first step towards real-time processing and distribution. Our findings demonstrate the potential for a global Earth-Ocean-Atmosphere-Space DAS monitoring network with multiple applications, e.g. marine mammal forecasting combined with ship tracking, to avoid ship strikes. By including automated processing and fusion with other remote-sensing data (automated identification systems, satellites, etc.), a low-cost ubiquitous real-time monitoring network with vastly improved coverage and resolution is within reach. We anticipate that this is a game-changer in establishing a global observatory for Ocean-Earth sciences that will mitigate current spatial sampling gaps. Our pilot test confirms the viability of this 'cloud-observatory' concept.

Main Text:

As awareness of the importance and complexity of the ocean environment becomes increasingly clear, the need for improved sensing, with better spatial resolution and increased temporal coverage, is now pressing (*6*). In this article, we demonstrate that standard Fibre-Optic (FO) telecommunication cables, of which there are already 1.2 million km that criss-cross the world's oceans (Figure 1, enough to wrap around the Earth 30 times), provide a means to continuously measure low-frequency acoustic events over large distances via Distributed Acoustic Sensing (DAS). DAS measures the optical back-scatter from impurities in the FO cables, but has so far not been used to collect data with such quality and range along the FO cable as we report here. With this increased range and signal quality, we show that such cables offer a unique potential for a cloud-based, global Earth-Ocean-Atmosphere-Space observatory that combines in-situ high spatial resolution DAS data from around the world with satellite and other remote sensing systems, a concept illustrated in Figure 1.

In recent work (*7*), Zhan et al. used State Of Polarisation (SOP) analysis to detect major earthquakes, measuring the integrated response along the entire 10,000 km length of the cable, but SOP cannot currently localise sources or benefit from beamforming. DAS can also be used to detect acoustic signals but, to the best of our knowledge, the farthest distance along a cable for which DAS has been reported is 43 km (*8*). We show here that it is now possible to interrogate and stream data from up to at least 120 km of FO cable at closely spaced intervals of a few metres, in near-real-time. This offers a unique opportunity for very high array gain over tens of thousands of discrete sensing elements with near-field beamforming and symmetry-breaking over curved sections of FO cable that can be applied to many topics in

Earth-Ocean-Atmosphere-Space monitoring. Existing FO cables, installed for an entirely different purpose can now be used to collect continuous monitoring data of high quality, over extended apertures, opening the door to massively increased spatial and temporal data coverage in previously inaccessible places, for very little additional cost compared to legacy approaches. This unlocks a new generation of capabilities, at a crucial time of need for improved global system monitoring.

We used approximately half of an existing submarine FO cable leg that runs from Longyearbyen to Ny-Ålesund in Svalbard, Norway, shown as the blue line in Figure 2. We connected the Longyearbyen end of the cable to an advanced DAS interrogator, streaming data from Svalbard to NTNU in near real-time. This represents both an innovation and a paradigm shift in how we can make distributed and coherent measurements in the future (with far simpler and cheaper sensory systems) moving the observatory itself to a virtual domain via web and cloud.

We have seen significant changes in oceanic soundscapes over recent decades (*9*), with anthropogenic ocean noise adding to a long list of stressors that impact marine life. The source characteristics of modern ships and their potential impact are still insufficiently characterised (*10*), but we can build on a recent DAS proof-of-concept from the Mediterranean Sea (*11*). Despite the clear importance of cetaceans (*12*,*13*) many species are still threatened or critically endangered, with insufficient data due to the difficulty of continuous monitoring (*14*). The challenge is that many cetaceans cover large, partly inaccessible habitats with long migratory routes (*15*), increasingly threatened by acoustic pollution, ship strikes, entanglement,

contaminants and climate change (*16*). These gaps exemplify our lack of adequate global detection and monitoring tools.

Results:

Ship and whale detection and tracking: During the sampling period, several ships passed close by and/or over the FO cable. One example is shown in Figure 3 (**A-C**) where we detected and tracked the Norbjørn, a general cargo ship proceeding SE at 11.7 kn. AIS position data reported by the ship are shown as a red line in Figure 3(**A**). Vessel positions estimated from the DAS data (white circles) correspond extremely well with the AIS track, with a root mean square deviation of only ±50 m. Positions are estimated from the hyperbolic wavefronts arising from the curved nearfield propagation to the FO cable visible on Figure 3(**B**), allowing near-field beamforming to determine both range and bearing (with a left-right ambiguity). We also detected the Doppler shift as the vessel crosses over the fibre, from which we estimated the vessel speed of 11.7 kn, in close agreement with the AIS data. The Doppler spreading is clearly seen modulating the ship's tonals in Figure 3(**C**).

To our knowledge, this is the first study that applies DAS for acoustic monitoring of baleen whales. Whale detections were made out to at least 95 km along the cable. We identified call types from at least two low-frequency baleen whale species: North Atlantic blue whale (*balaenoptera musculus*) and fin whale (*balaenoptera physalus*), with a number of stereotyped North Atlantic blue whale signals (AB call, peak frequency at ~16.9 Hz; arched sounds, 9-Hz call (*17*)) and mid-frequency down-sweeps (peak frequency ~45 ± 15 Hz, average duration 5.4 ± 2.4 s). Down-sweep calls were the most common and can be attributed to blue whales (AB

and D-calls), fin whales (D- calls or pulses), but also sei whales (*balaenoptera borealis*) (*18*). Blue whale stereotyped calls were recorded during the entire recording period with a higher number of calls detected after 2020.07.23. In four instances, sightings from whale-watching tours confirmed the presence of a blue whale in the area.

Figure 3(**D**) shows an example from within Isfjorden on 2020.06.27 at 17:35 UTC in which hyperbolic wavefront arrivals, whose apex indicate the point on the FO cable closest to the source, can be seen from two distinct whales, at 37.2 and 39.4 km. The. Figure 3(**E-F**) show spectrograms of the signals from the two whales with their respective waveforms obtained from beamforming. A stereotyped Atlantic blue whale call can be seen in Figure 3(**E**) before 10 s, and arched sounds around 10 s and 78 s. Figure 3(**F**) shows a short downsweep, more likely from a fin whale. The high spatial resolution and extent of FO cables offer a complementary sensing modality to other cetacean monitoring techniques, including the ability to determine both range and bearing to animals, separating individuals aurally and spatially (Audio S1) and with the potential to track the movement of vocalising whales over continuous time periods over long distances.

Earthquakes: We analysed seismic signals from a local and a teleseismic earthquakes at distances of ~100 and ~5100 km, respectively, from the FO cable. These are depicted in Figure 2 together with the region's seismicity. We observe different wave types (compressional and shear) excited in the ocean sub-bottom that correspond to these seismic events as described in (*19*). As in previous studies (*5,8,20,21*), our DAS analysis shows a rich expression of natural features, from 0.01−20 Hz, capturing not only the range and direction of earthquake hypocentres, but also the effect of deeper-diving waves passing through regions of higher

velocity, and the interaction with local bathymetry. We demonstrate that source localisation, exploiting the long array with a massive number of sensing points, represents a valuable complement to conventional methods. These results can be found in supplementary materials (Fig. S1–S4).

Storms and ocean swell: Figure 4(**A**–**D**) display spectrograms of 21 days of data at four different points along the FO cable, showing nearly-linear narrow-band dispersion trends with different gradients, ranging from 0.04−0.10 Hz over several days. These trend lines are generated by ocean surface gravity waves from distant storms. The trend lines were also observed in the data recorded by a conventional ocean bottom sensor (*22*). Figure 4(**E**) shows wind measurements at two weather stations: Isfjord Radio, which is at ~55 km from the entrance of the fjord and Longyearbyen airport, where the cable begins.

We observe that the trend lines increase monotonically and linearly in frequency over time. During the entire 44-day recording period, we can easily identify 12 such trends in the time-frequency spectra. Each of these events typically lasts for 50-100 hours, with some overlapping. The amplitude level of these events increases towards the inner parts of the fjord, which implies that the fjord acts as a narrowing amplifier for this type of signal.

Four linear trends corresponding to distant storms are highlighted in Figure 4(**D**). We used the time-frequency gradient to calculate great-circle distances and travel times of the storm-induced ocean surface gravity waves from the storm centre to the DAS array, allowing us to trace all four events back to the generating storms. Event 1 corresponds to the Tropical Storm Edouard ~4100 km from Longyearbyen, occurring on 2020.07.04–06 (*23*). Event 2 probably corresponds to a storm offshore south Brazil at ~13,000 km on 2020.07.01–07, although a lack

of satellite storm tracking data from the Southern Atlantic prevents unambiguous identification. Event 3 corresponds to an extra-tropical depression between Iceland and Greenland at ~2400 km on 2020.07.16–18. Finally, Event 4 is associated with a storm offshore south Brazil at ~11,000 km distance from the array.

Discussion:

The wide range of valuable monitoring capabilities that DAS now offers, especially if extended to near-continuous monitoring over many FO cables, spanning the globe, is a game-changer. To realise the potential of a cloud-based global observatory illustrated in Figure 1 will require data management and automated real-time analysis on an unprecedented scale. The 120 km length of FO cable sampled for this work generated ~7 TB of data a day.

The ship example shows that vessels passing over or near a FO cable can be detected and tracked, using near-field beamforming, and that there is even a potential to characterise the acoustic signature and directionality, including identification, if signals are routinely acquired from an array of FO cables, augmented by AIS data.

The baleen whale example further shows that the high SNR gain available from extended aperture array processing can be used to construct high-quality audio waveforms. We expect to be able to detect whale vocalisations for distances along a FO cable in excess of 100 km. DAS, combined with AIS and other data streams, could generate real-time whale- and ship-tracking with early warning and alert systems broadcasted over the existing AIS system to vessels that could then reduce the risk of ship-strike injuries, recognised as one of the most critical anthropogenic threats to cetaceans (*16*) and anthropogenic noise impacts, a considerable, yet difficult-to-manage threat to cetacean populations (*24*).

The earthquake studies demonstrate the possibility to use FO cables to estimate the ratio of compressional to shear wave velocities, v_p/v_s, from different segments along the cable. In addition, DAS reveals ultra-low frequency (~0.01 Hz) microseisms and ocean gravity waves from local and distant storms.

In conclusion, we believe that DAS has now reached a performance level that offers a disruptive capability in global Earth-Ocean-Atmospheric-Space monitoring, providing a hitherto unimaginable spatial coverage and resolution, combined with continuous data streaming. The broader implications include:

- Long-term climate monitoring – DAS could provide spatial and temporal dimensions to complement other measurement schemes, 'averaging out' point sampling noise in space and time to give more accurate measurements of small changes, as was achieved with satellite altimetry and GPS by using many passes to get mm accuracy of position, sea and terrain heights. It could also be possible to monitor ice processes such as fracturing and calving in the Arctic.
- Long-term monitoring of CO_2 sequestration reservoirs. CO_2 sequestration is an important element in the energy transition and move to decarbonise. DAS has already been applied for CO_2 storage monitoring to map CO_2 plumes at two pilot projects (*25*). A combination of downhole and seabed horizontal fibres has a great potential for reducing monitoring costs compared to conventional time lapse seismic.
- Atmosphere-Ocean interactions – A topic that is still not fully understood, where DAS offers something new in its ability to continuously monitor long ocean swells from storms with global coverage.
- Monitoring the ocean soundscape – DAS can sample in places where there has been little interest or resource support, e.g. off the coasts of South America and Africa, mitigating geospatial and societal biases in observations in line with UN development goal 9.5, enhancing scientific research and upgrading technological capabilities and applications, particularly in developing countries, and UN goal 14.a; improvement of ocean health and enhance biodiversity in developing countries.
- Big Data – DAS offers the potential of collecting a truly Big Data set, with extensive spatial and temporal coverage, ripe for exploitation by data mining and AI to reveal global patterns. Because DAS simultaneously measures processes occurring in the atmosphere, ocean and solid earth below, there is the potential to discover cross-disciplinary interactions and global patterns between meteorologists, oceanographers and geophysicists.

The biggest challenges lie in improving the SNR and range capabilities, the availability of dark fibres (or the ability to use 'live' fibres), reducing the cost of interrogators, data management, and applying automated detection and classification methods. None of these challenges are without solutions and work is rapidly pushing back the boundaries of what is

possible, which will lead to a near-future breakthrough in continuous, distributed environmental sensing over the majority of the planet's surface.

References

1. Editorial, Introduction to the special issue: The global state of the ocean; interactions between stresses, impacts and some potential solutions. Synthesis papers from the International Programme on the State of the Ocean 2011 and 2012 workshops. *Marine Pollution Bulletin* **74**, 491-494 (2013).

2. J. Bijma, H. O. Pörtner , C. Yesson , Alex D. Rogers, Climate change and the oceans – What does the future hold? *Marine Pollution Bulletin* **74**, 495-505 (2013).

3. W. Munk, The U.S. commission on the Ocean Policy Testimony. San Pedro, California April 2002.

4. A. Sladen, D. Rivet, J. P. Ampuero, L. De Barros, Y. Hello, G. Calbris, P. Lamare, Distributed sensing of earthquakes and ocean-solid Earth interactions on seafloor telecom cables. Nature Communications 10:57777 (2019).

5. N. J. Lindsey, E. R. Martin, D. S. Dreger, B. Freifeld, S. Cole, S. R. James, B. L. Biondi, J. B. Ajo-Franklin, Fiber-optic network observations of earthquake wavefields. *Geophysical Research Letters* **44**, 11,792–11,799 (2017).

6. B. M. Howe, J. Miksis-Olds, E. Rehm, H. Sagen, P. F. Worcester, G. Haralabus, Observing the oceans acoustically. *Frontiers in Marine Science* **6**, 426 (2019).

7. Z. Zhan, M. Cantono, V. Kamalov, A. Mecozzi, R. Müller, S. Yin, J. C. Castellanos, Optical polarization-based seismic and water wave sensing on transoceanic cables. *Science* **371**, 931–936 (2021).

8. E. F. Williams, M. R. Fernández-Ruiz, R. Magalhaes, R. Vanthillo, Z. Zhan, M. González-Herráez, H. F. Martins, Distributed sensing of microseisms and teleseisms with submarine dark fibers. *Nature communications* **10**, 5778 (2019).

9. N. Jones, The quest for quieter seas. *Nature* **568**, 158–161 (2019).

10. R. Williams, D. Cholewiak, C. W. Clark, C. Erbe, C. George, R. Lacy, R. Leaper, S. Moore, L. New, C. Parsons, H. Rosenbaum, T. Rowles, M. Simmonds, R. Stimmelmayr, R. S. Suydam, A. Wright, Chronic ocean noise and cetacean population models. *J. Cetacean Res. Manage.* **21**, 85–94 (2020).

11. D. Rivet, B. de Cacqueray, A. Sladen, A. Roques, G. Calbris, Preliminary assessment of ship detection and trajectory evaluation using distributed acoustic sensing on an optical fiber telecom cable. *The Journal of the Acoustical Society of America* **149**, 2615–2627- (2021).

12. J. Roman, J. A. Estes, L. Morissette, C. Smith, D. Costa, J. McCarthy, J. B. Nation, S. Nicol, A. Pershing, V. Smetacek, Whales as marine ecosystem engineers. *Frontiers in Ecology and the Environment* **12**, 377–385 (2014).

13. A. J. Pershing, L. B. Christensen, N. R. Record, G. D. Sherwood, P. B. Stetson, The impact of whaling on the ocean carbon cycle: Why bigger was better. *PLoS ONE* **5**, e12444 (2010).

14. IUCN – SSC Cetacean Specialist Group, Status of the World's cetaceans. (2021).

15. H. Bailey, B. R. Mate, D. M. Palacios, L. Irvine, S. J. Bograd, D. P. Costa, Behavioural estimation of blue whale movements in the Northeast Pacific from state-space model analysis of satellite tracks. *Endangered Species Research* **10**, 93–106 (2010).

16. P. O. Thomas, R. R. Reeves, R. L. Brownell Jr, Status of the world's baleen whales. *Marine Mammal Science* **32**, 682–734 (2016).

17. D. K. Mellinger, C. W. Clark, Blue whale (Balaenoptera musculus) sounds from the North Atlantic. *The Journal of the Acoustical Society of America* **114**, 1108–1119 (2003).

18. H. Ou, W. W. Au, S. Van Parijs, E. M. Oleson, S. Rankin, Discrimination of frequency-modulated Baleen whale downsweep calls with overlapping frequencies. *The Journal of the Acoustical Society of America* **137**, 3024–3032 (2015).

19. T. Saito, H. Tsushima, Synthesizing ocean bottom pressure records including seismic wave and tsunami contributions: Toward realistic tests of monitoring systems. *Journal of Geophysical Research: Solid Earth* **121**, 8175–8195 (2016).

20. P. Jousset, T. Reinsch, T. Ryberg, H. Blanck, A. Clarke, R. Aghayev, G. P. Hersir, J. Henninges, M. Weber, C. M. Krawczyk, Dynamic strain determination using fibre-optic cables allows imaging of seismological and structural features. *Nature communications* **9**, 2509 (2018).

21. J. B. Ajo-Franklin, S. Dou, N. J. Lindsey, I. Monga, C. Tracy, M. Robertson, V. R. Tribaldos, C. Ulrich, B. Freifeld, T. Daley, X. Li, Distributed acoustic sensing using dark fiber for near-surface characterization and broadband seismic event detection. *Scientific reports* **9**, 1328 (2019).

22. P. D. Bromirski, F. K. Duennebier, The near-coastal microseism spectrum: Spatial and temporal wave climate relationships. *Journal of Geophysical Research: Solid Earth* **107**, ESE 5-1–ESE 5-20 (2002).

23. R. J. Pasch, National hurricane center tropical cyclone report: Tropical storm Edouard (AL052020), *Tech. rep.*, National Oceanic and Atmospheric Administration (2021).

24. R. P. Schoeman, C. Patterson-Abrolat, S. Plön, A global review of vessel collisions with marine animals. *Frontiers in Marine Science* **7**, 292 (2020).

25. P. Ringrose, A-K. Furre, S.M.V. Gilfillan, S. Krevor, M. Landrø, R. Leslie, T. Meckel, B. Nazarian, A. Zahid, Storage of Carbon Dioxide in Saline Aquifers: Physicochemical Processes, Key Constraints, and Scale-Up Potential, *Annual Review of Chemical and Biomolecular Engineering*, **12**, 471-494, (2021).

26. O. H. Waagaard, E. Rønnekleiv, A. Haukanes, F. Stabo-Eeg, D. Thingbø, S. Forbord, S. E. Aasen, J. K. Brenne, Real-time low noise distributed acoustic sensing in 171 km low loss fiber. *OSA Continuum* **4**, 688–701 (2021).

27. A. H. Hartog, *An Introduction to Distributed Optical Fibre Sensors* (CRC Press, ed. 1, 2017).

28. T. Nishimura, K. Emoto, H. Nakahara, S. Miura, M. Yamamoto, S. Sugimura, A. Ishikawa, T. Kimura, Source location of volcanic earthquakes and subsurface characterization using fiber-optic cable and distributed acoustic sensing system. *Scientific reports* **11**, 6319 (2021).

29. F. Ardhuin, T. H. C. Herbers, Noise generation in the solid Earth, oceans and atmosphere, from nonlinear interacting surface gravity waves in finite depth. *Journal of Fluid Mechanics* **716**, 316–348 (2013).

30. G. B. Airy, Tides and waves, *Encyclopaedia Metropolitana (1817–1845)* (London, 1841), *Mixed Sciences*, vol. 3.

31. A. D. D. Craik, The origins of water wave theory. *Annual Review of Fluid Mechanics* **36**, 1–28 (2004).

32. H. Matsumoto, S. Inoue, T. Ohmachi, Dynamic Response of Bottom Water Pressure due to the 2011 Tohoku Earthquake. *Journal of Disaster Research* **7**, 468–475 (2012).

33. M. Landrø, P. Hatchell, Normal modes in seismic data — Revisited. *GEOPHYSICS* **77**, W27–W40 (2012).

34. J. Lin, S. Fang, X. Li, R. Wu, H. Zheng, Seismological observations of ocean swells induced by typhoon Megi using dispersive microseisms recorded in coastal areas. *Remote Sensing* **10**, 1437 (2018).

35. W. H. Munk, G. R. Miller, F. E. Snodgrass, N. F. Barber, G. E. R. Deacon, Directional recording of swell from distant storms. *Philosophical Transactions of the Royal Society of London. Series A, Mathematical and Physical Sciences* **255**, 505–584 (1963).

Acknowledgments: The authors would like to acknowledge the invaluable support of Tim Cato Netland and Daniel Bergh in the downloading of data from the NTNU server.

Funding:

HJK and LB are funded by the Research Center for Arctic Petroleum Exploration (ARCEx) partners, and the Research Council of Norway (Grant No. 228107).

KT and RAR are funded by the GAMES consortium at NTNU (Research Council of Norway; Grant No. 294404).

ML, JRP, and SEJ receive research funding from the Centre of Geophyscial Forecasting (CGF) at NTNU, sponsored by Grant No. 309960 (Norwegian Research Council).

The acquisition of the data was financed by ARCEx and GAMES.

Author contributions:

ML, JKB, AH, SEJ, OS, and FS designed the work.

AH and FS collected the DAS data.

KT, LB and RAR processed data.

LB, JRP and ML analysed the ship data.

HJK, LB and JRP analysed the whale data.

RAR, KT and ML analysed the earthquake data.

KT, ML and JRP analysed the microseism data.

All authors participated in the data interpretation and writing.

Competing interests: There are no competing interests related to this work.

Materials & Correspondence: DAS data are available upon request to the corresponding author (martin.landro@ntnu.no). AIS data obtained from Kystdatahuset data provider https://kystdatahuset.no. Whale sighting data provided by Svalbard adventures Turproduksjon https://svalbardadventures.com and Henningsen Transport & Guiding https://www.svalbardcruise.com. Seismic data from the station at Svalbard are available IRIS web Services: https://service. iris.edu/. Details on the Alaska earthquake available at: https://earthquake.usgs.gov/earthquakes/eventpage/us7000asvb/executive. Historic seismic data near Svalbard available at: https://www.norsar.no/seismic-bulletins/ and http://nnsn.geo.uib.no/nnsn/#/data/events/bulletins.

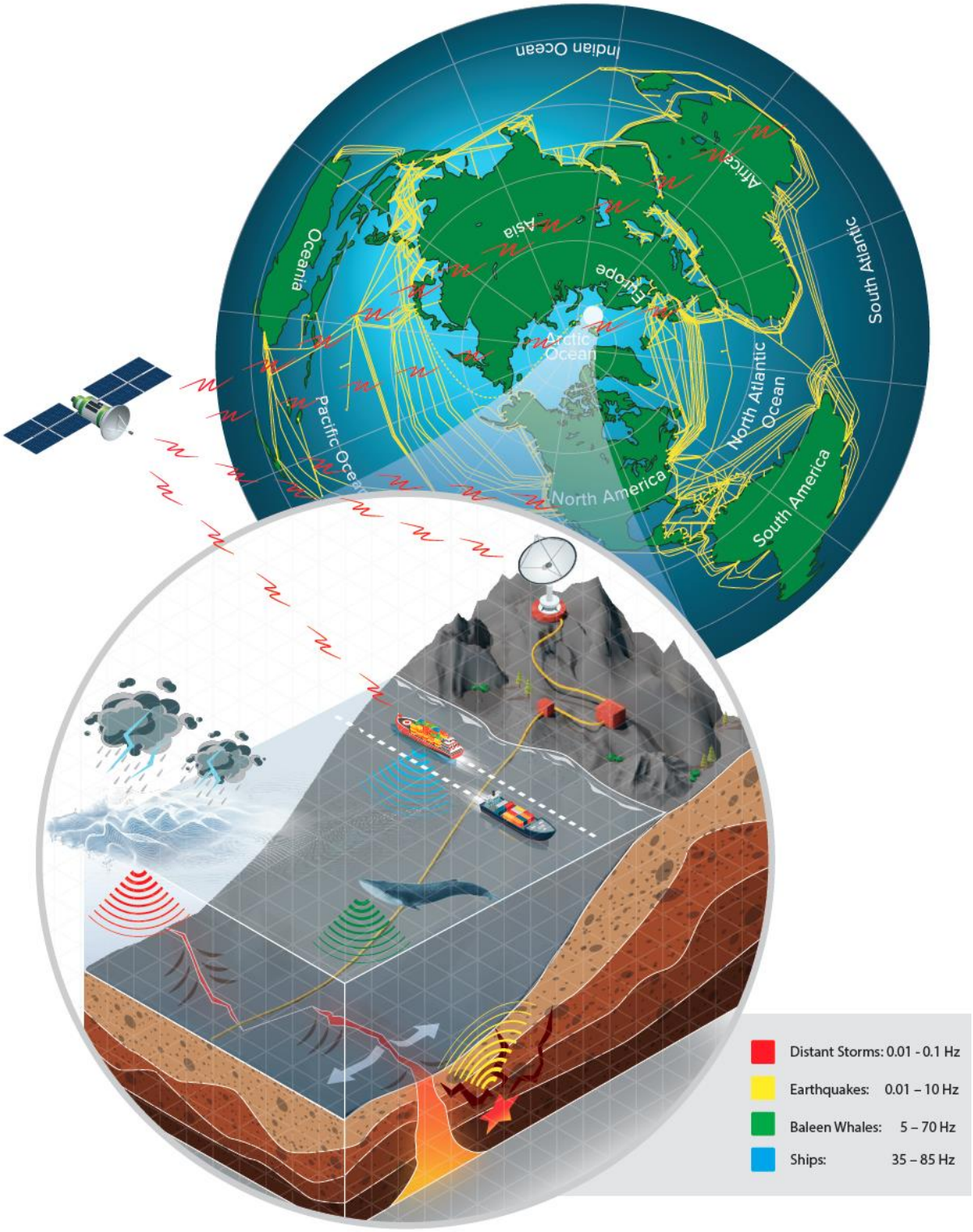
Indian Ocean
Africa
Asia
Europe
Oceania
South Atlantic
Arctic Ocean
North Atlantic Ocean
Pacific Ocean
North America
South America
Distant Storms: 0.01 - 0.1 Hz
Earthquakes: 0.01 – 10 Hz
Baleen Whales: 5 – 70 Hz
Ships: 35 – 85 Hz

Fig. 1. Earth-Ocean-Atmosphere-Space observatory concept. North polar stereographic projection of the world in the upper-right-hand globe, showing the extensive network of existing Fibre-Optic (FO) cables (yellow lines). The lower-left zoomed inset illustrates the key features of the observatory and its capabilities, including the DAS detection, tracking and identification of whales, ships, storms and earthquakes, processed in real-time, fused with other sensing sources such as satellite-derived Automated Identification System data from ships and relayed to the cloud. The frequencies associated with the various sources are those used in this paper whereas actual phenomena span a much wider frequency range, and indeed DAS can be used up to at least 5 kHz.

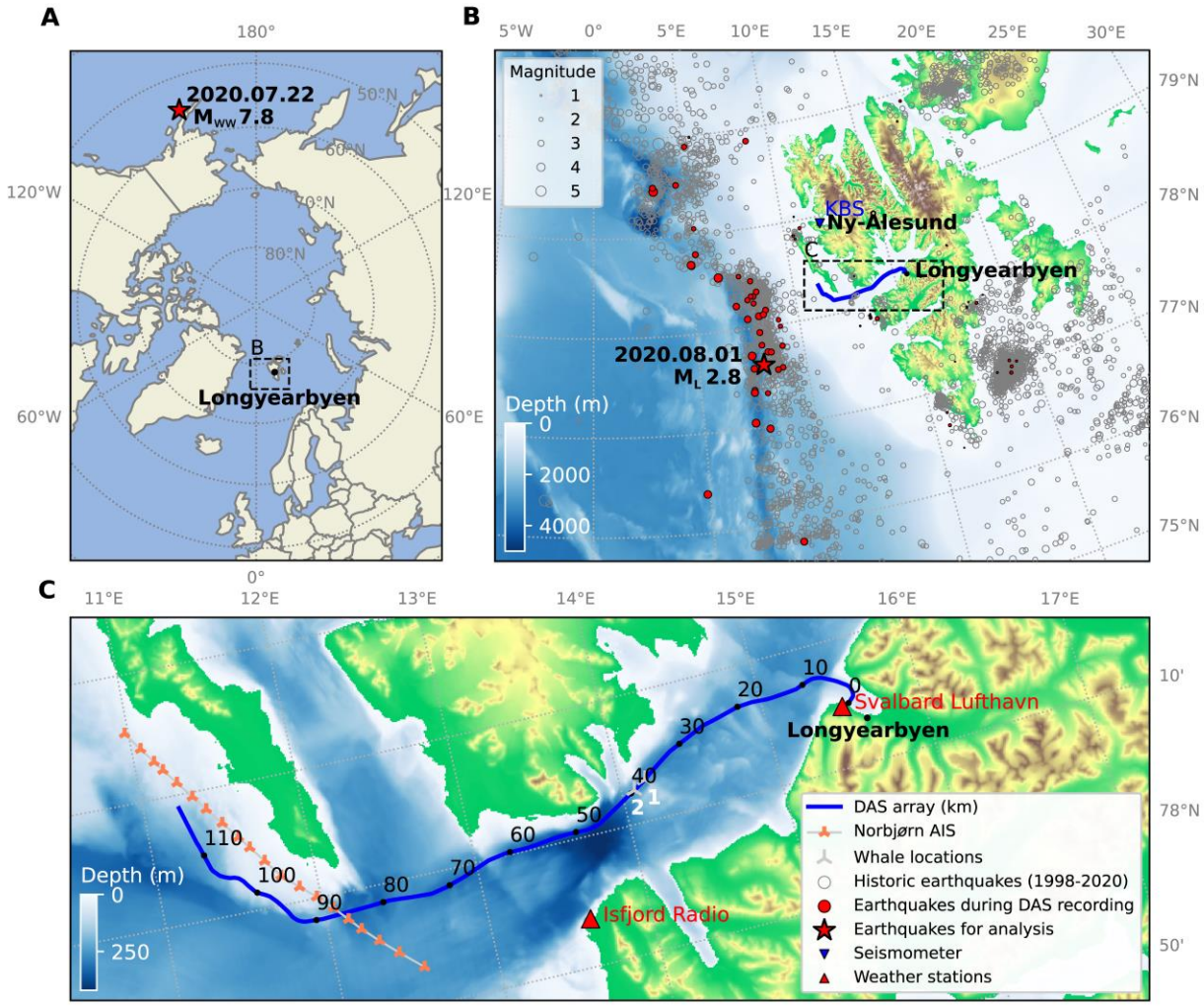

Fig. 2. Geographical locations. (**A**) A polar stereographic map of the Arctic showing the epicentre of the M_{ww} 7.8 teleseismic earthquake in Alaska on 2020.07.22 and the location of our FO array, near Longyearbyen. (**B**) A regional map illustrating the epicentres of the M_L 2.8 earthquake in the mid-Atlantic ridge on 2020.08.01 and other recorded earthquakes between 1998–2020. (**C**) A local map showing 120 km of the underwater DAS array from the shore at Longyearbyen.

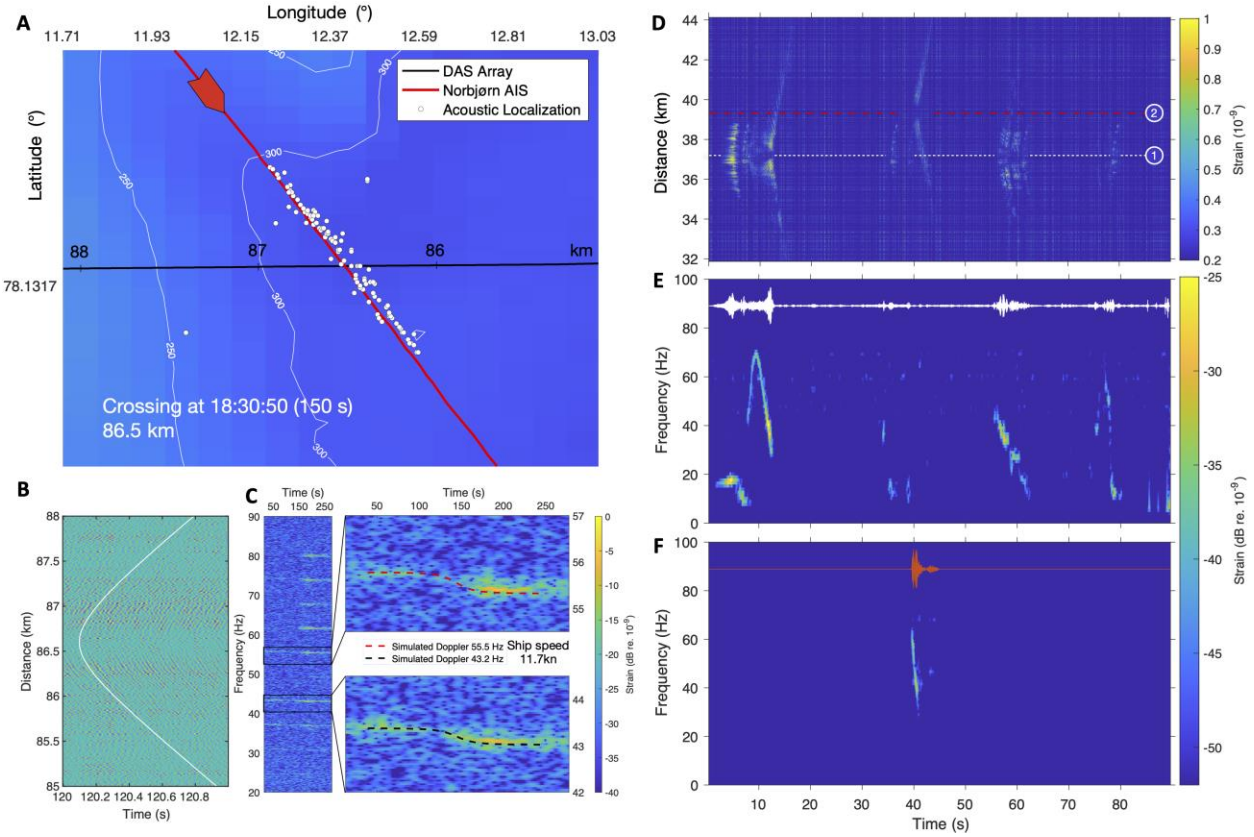

Fig. 3. **DAS detection, localisation, tracking and identification of a ship (A-C) and two whales (D-F). (A-C)** General cargo ship Norbjørn was tracked as it headed SE at 11.7 kn in 300 m of water around 86.5 km of FO cable. (**A**) Comparison between acoustic localisation and Automatic Identification System (AIS) track. Norbjørn's acoustic signature (**B**) in the space-time domain at the time of crossing, shows hyperbolic wavefronts used for acoustic localization (**C**) spectrogram, at 160 m from the crossing point, varies in time due to the Doppler effect. **(D–F)** Baleen whale calls over 12 km of FO cable (**Audio S1**). (**D**) Space-time representation used for identification and acoustic source separation: Whale 1 was at 37.2 km and Whale 2 was at 39.4 km. (**E&F**) Waveforms and associated spectrograms after beamforming and source separation: Whale 1 (**E**)

show a vocal repertoire characteristic of North Atlantic blue whales (19) plus some likely-social D-calls (30–70 s) while the signal from Whale 2 (**F**) could be attributed to a fin whale.

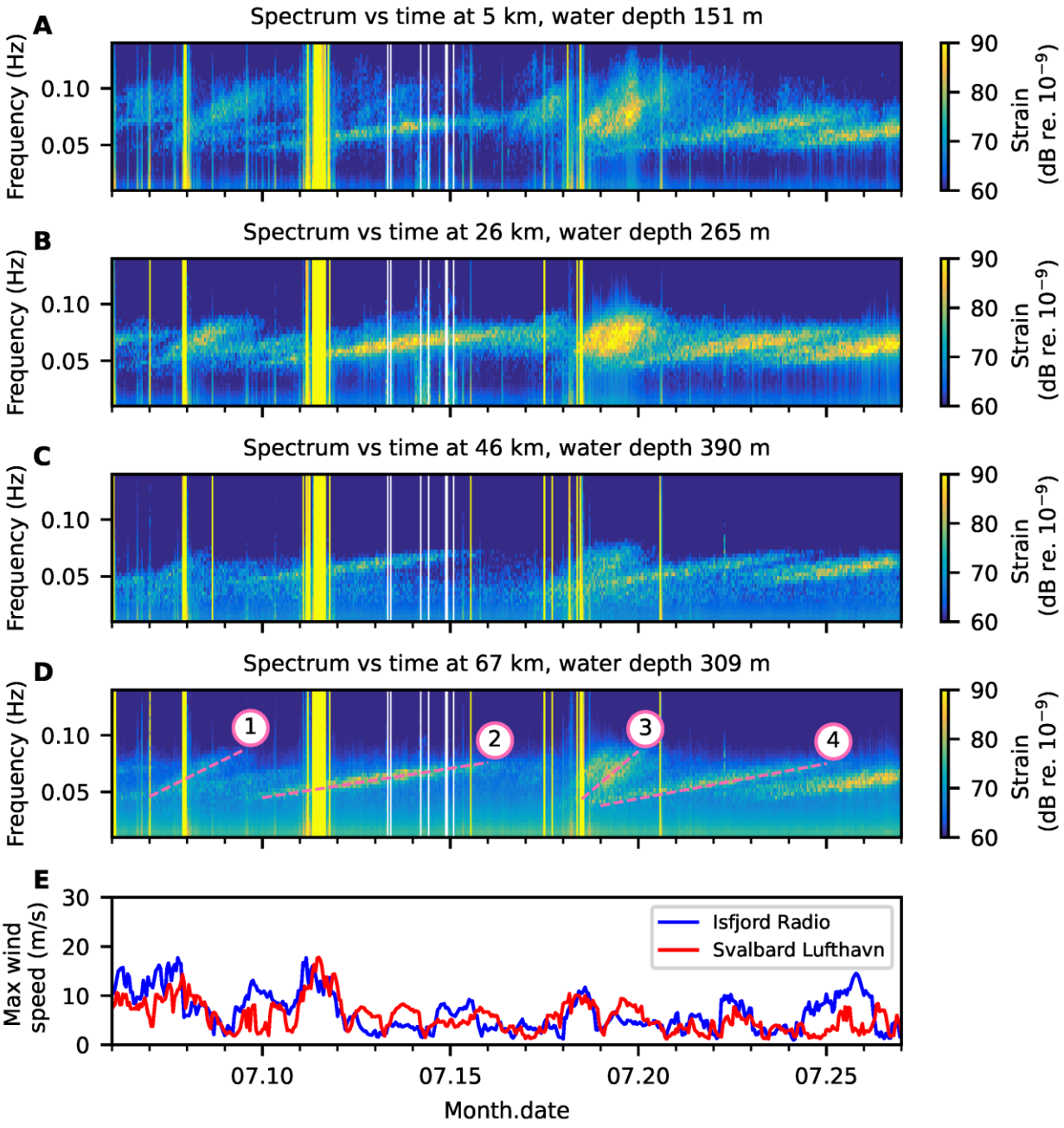

Fig. 4. Atlantic Ocean storms observed from DAS. Spectrogram at 5, 26, 46 and 67 km of FO cable (**A**–**D**). Yellow vertical stripes are due to saturation, while the white vertical stripes were caused by data drop-out in the communication with NTNU. The bottom panel (**E**) shows the

associated maximum wind speed measured at Isfjord Radio and Svalbard Lufthavn weather stations (Fig.2). Four storm events marked in (D) are discussed in texts.

METHODS

We used a dark (SMF-28 single mode silica) fibre in an existing Uninett submarine telecommunication cable, trenched 1 to 2 m into soft sediment, running from Longyearbyen to Ny-Ålesund in Svalbard, Norway. We connected the Longyearbyen end of this cable to an Alcatel Submarine Networks 'OptoDAS' interrogator, streaming data from Svalbard to NTNU in near-real-time via the Uninett network by using the 1 Gbit/s network interface on the Alcatel interrogator. The OptoDAS interrogator injected linear frequency-modulated optical pulses (*26*) which are back-scattered by anomalies in the fibre. The interrogator calculates the time-differentiated phase change of the back-scattered response from consecutive sweeps for each sampled fibre position. The time-differentiated phase change can be converted to the longitudinal strain of the corresponding fibre section (*27*). In this experiment, we used light pulses of 1550 nm free-space wavelength to sample 30,000 channels with 4.08 m spacing from 0 to 120 km along the cable. The gauge length used was 8.16 m, providing 8.16m resolution along the cable. The signal strength decays along the cable such that the returned signal strength from 100 km is ~ −40 dB with respect to 1 km. The DAS data were continuously sampled over 44 days and streamed over Uninett's research network to NTNU in Trondheim, where they were recorded at 645.16 Hz, providing just over 300 Hz of bandwidth.

For ship tracking, vessel positions were estimated by optimising the cross-correlation of observed time-of-arrival on 2-second time windows with predicted time of arrival along the FO cable at 16 m spacing for an array of candidate positions. The usual left-right ambiguity associated with linear arrays was suppressed by choosing the solution that matches the AIS track, but could in principle have been resolved by the asymmetry in bathymetry or the vessel's acoustic directivity.

For the earthquake analyses, we used several processing tools (band-pass filtering, FK-filtering, FX domain swell noise attenuation, and FX deconvolution) in addition to beamforming to increase the SNR of the recorded signal and better extract P- and S-wave phase arrival times. When beamforming, we first estimated the apparent velocity and angle. Then we used these values to find the optimal number of traces that could be stacked coherently for different segments of the cable. In this way we were able to increase the SNR for a segment of the FO cable (61 km along the channel) from 10.7 dB to 30.5 dB for the P-wave signal and 20.4 dB to 40.6 dB for the S-wave signal (Figure S2).

Supplementary Alaska and local earthquake.

On 2020.07.22 at 06:12:44 UTC an M_{ww} 7.8 earthquake occurred approximately 100 km south of the Alaska Peninsula at a depth of 28 km. The earthquake was recorded at seismic stations worldwide including our DAS array near Longyearbyen, ~5100 km away from the epicentre on a great circle. Figure 2(**A**) shows the location of this earthquake, while the inset (**B**) shows the DAS array and the KBS seismic station, belonging to the Global Seismograph Network (GSN), at Ny-Ålesund. The DAS data have similar characteristics to the east-west vibrating component recorded by the KBS seismometer. Figure S1(**A**) compares the seismogram from a single DAS channel (top) at 36 km distance from the shore with a stacked version (middle) from the sum of 25 neighbouring traces, and the seismogram from the KBS east-west component (bottom). There is an excellent correspondence of P, S and SS arrivals between the data from DAS and the KBS component. Stacking 25 traces increases the SNR of the DAS data by ~ 3 dB, still below the 34 dB SNR offered by the KBS seismometer. The advantage of DAS over a conventional seismometer lies in

the length of the array of sensors, in this case 120 km. With such an extended array, we can visualise teleseisms in a space-time display, where coherent teleseismic events are easily observed and distinguished. Here, we emphasise that by analysing the 2D profile we can easily identify the surface waves corresponding to the Alaska earthquake and a separate P wave arrival from another source, hardly distinguished in the KBS east-west seismogram.

A local M_L 2.8 earthquake with epicentre close to the Mid-Atlantic ridge occurred on 2020.08.01 at 02:54:00 UTC. Figure S1(**B**) shows the signal in the space-time domain. The earthquake seismic waves arrive at the FO cable from a nearly-orthogonal direction compared to the Alaska teleseism, which arrives from a broadside direction. This offers a unique possibility to compare array effects and analyse apparent velocities for P and S waves from the two earthquakes. For the local earthquake, we find that the apparent velocity and the ratio of P- to S-wave velocities (v_p/v_s) increases with the distances from the epicentre to the DAS sensors. This is due to energy propagation eigenpaths travelling at increasing depth to reach sensor points at increasing distance from the epicentre.

Because the Atlantic earthquake is closer to the cable (110–190 km away) compared to the Alaska earthquake (5100 km away), we can use the relatively long array (120 km) to estimate the position of the Atlantic earthquake, which is then compared with the position reported by the Norwegian National Seismic Network (NNSN) and NORSAR. We applied an optimisation algorithm to estimate the epicentre, which resulted in a location in close agreement (~10 km) with that reported by NNSN and NORSAR. Previously, Jousset et al. (*20*) relocated a local earthquake using DAS, while Nishimura et al. (*28*) located volcanic earthquakes using DAS and grid search methods. Nevertheless, to the best of our knowledge, this is the first example of using DAS data

from a 100+ km-long FO cable to localise an earthquake (Figure S3). The long antenna offered by FO cables, especially if they are curved, offers a unique complementary method to traditional source localisation for earthquakes and other seismic sources.

We also analysed the data down to a frequency of 0.01 Hz, which reveals additional environmental insights. Figure (Figure S4) shows three power spectral density levels from 0.01–20 Hz, computed over three different 300 s time windows. The DAS data in Figure S4(**A**) contain no known significant earthquakes. Therefore, this time window represents background microseismic noise. Figure S4(**B**) contains the primary P-wave arrivals from the M_{ww} 7.8 teleseismic earthquake from Alaska on 2020.07.22. The spectrum in Figure S4(**C**) is computed from a time window that contains the primary P-wave and S-wave arrivals from the M_L 2.8 earthquake from the mid-Atlantic ridge on 2020.08.01.

In the background microseismic noise data in Figure S4(**A**), we clearly see two types of signals. The first is the so-called primary microseism, with frequencies from ~0.04–0.10 Hz, whose spectral density is independent of water depth. This signal is generated by variations in the loading pressure associated with sea surface height. It is, therefore, a hydrostatic response associated with ocean surface gravity waves excited by winds or a nonlinear wave-wave interaction mechanism (*28*). The phase velocity (c_p) of an ocean surface gravity wave is formulated as $c_p = \omega/k$, where the well-known dispersive relation (*30*,*31*) is $\omega^2 = gk \tanh(kH)$, ω is the angular frequency, k is the angular wavenumber, and H is the water depth. The second signal type has higher frequencies, ranging from ~1–10 Hz, and it is strongly correlated with the water depth. We interpret this signal to be an acoustic resonance of the water column (*32*). This dispersive hydroacoustic wave has cutoff frequencies for the rigid ocean bottom given by $f_n = (2n - 1)c/(4H)$, where n is an integer

mode order and c is sound speed in the water column (*33*). The primary microseism and the fundamental mode (n = 1) of the acoustic resonance can be observed in Figure S4(**A**). The excitation mechanisms of the ocean bottom corresponding to different wave types are described in (*19*). The primary microseism (~0.04–0.10 Hz) and the hydrodynamic response (~0.1–1.0 Hz) show no correlation to the water depth, while the normal modes (~1–10 Hz) show a strong correlation to the water depth.

The number of excited modes typically increases for forcing signals with higher horizontal wavenumbers and with stronger acoustic sources. In Figure S4(**A**), we interpret the first high-amplitude event as the first normal mode, and the source is most probably non-linear wave-wave interaction of long ocean waves, or minor earthquakes or other signals coming from the earth, or a combination of these. With the additional significant seismic energy in Figures S4(**B, C**), the hydroacoustic waves are stronger, and the higher modes of the acoustic resonance are more visible than those revealed by the background microseismic noise alone. In addition, the sea bottom pressure variation is accentuated when the seismic P-waves arrive. This hydrodynamic response can be observed between ~0.1–1.0 Hz, as clearly shown in Figure S4(**B**). Additionally, in Figure S4(**B**), we see that the Alaska earthquake leads to a significant amplitude increase, but with a similar number of excited modes as for the background microseismic noise. However, the mid-Atlantic earthquake in Figure S4(**C**) shows a larger number of excited normal modes, which attribute to the wave containing higher horizontal wavenumbers arising because the source direction was nearly in-line with the FO cable. The levels are also lower than those in the Alaska signal in Figure S4(**B**). Our DAS analysis therefore shows a rich expression of natural features, from 0.01−20 Hz, capturing not only the range and direction of earthquake hypocentres, but the

effect of deeper-diving waves passing through regions of higher velocity, and the interaction with local bathymetry.

For the distant storm analysis, we used the method given by (*34*) based on (*35*), whereby the time-frequency gradient can be used to calculate great-circle distances and travel times of the storm-induced ocean surface gravity waves from the storm centre to the DAS array.

Extended data:

Figs. S1 to S5

Audio S1 to S2

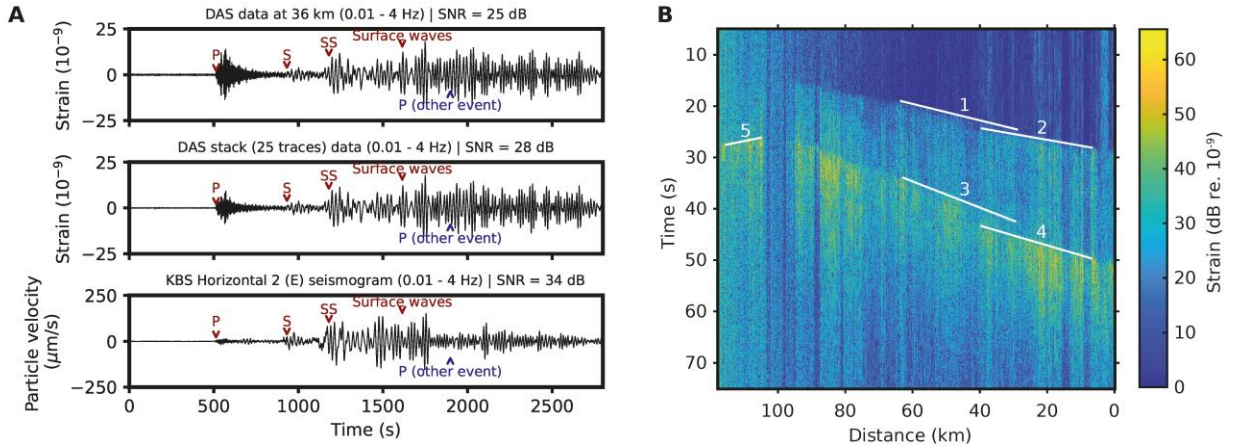

Fig. S1.

Seismic signals from a teleseismic Alaska earthquake (A) and a local mid-Atlantic earthquake (B). (A) shows a single DAS channel at 36 km (top), a stacked waveform using 25 traces around the 36 km channel (middle) and the east-west component from the KBS seismic station (bottom). (B) shows the local mid-Atlantic ridge earthquake signal over the entire 120 km long cable (plotted as time after origin time; **Audio S2**). The P- and S-waves are clearly visible. At approximately 22 km distance we observe a 15–20 km "pinch out" for both the P and S waves and different apparent velocities for different parts of the cable (white lines). Correcting for the apparent angle (~172.3˚) the apparent velocity of the pinch-out is 8.66 km/s (2) and 5.14 km/s (4), while the other observed apparent velocities are 6.21 km/s (1) and 3.76 km/s (3) with a correction angle of ~175.3˚. These values correspond to v_p/v_s ratios of 1.69 and 1.65, respectively. A third apparent S-wave velocity can be observed at the far end of the cable (5) with an apparent velocity of 2.23 km/s (correction angle of ~287.3˚).

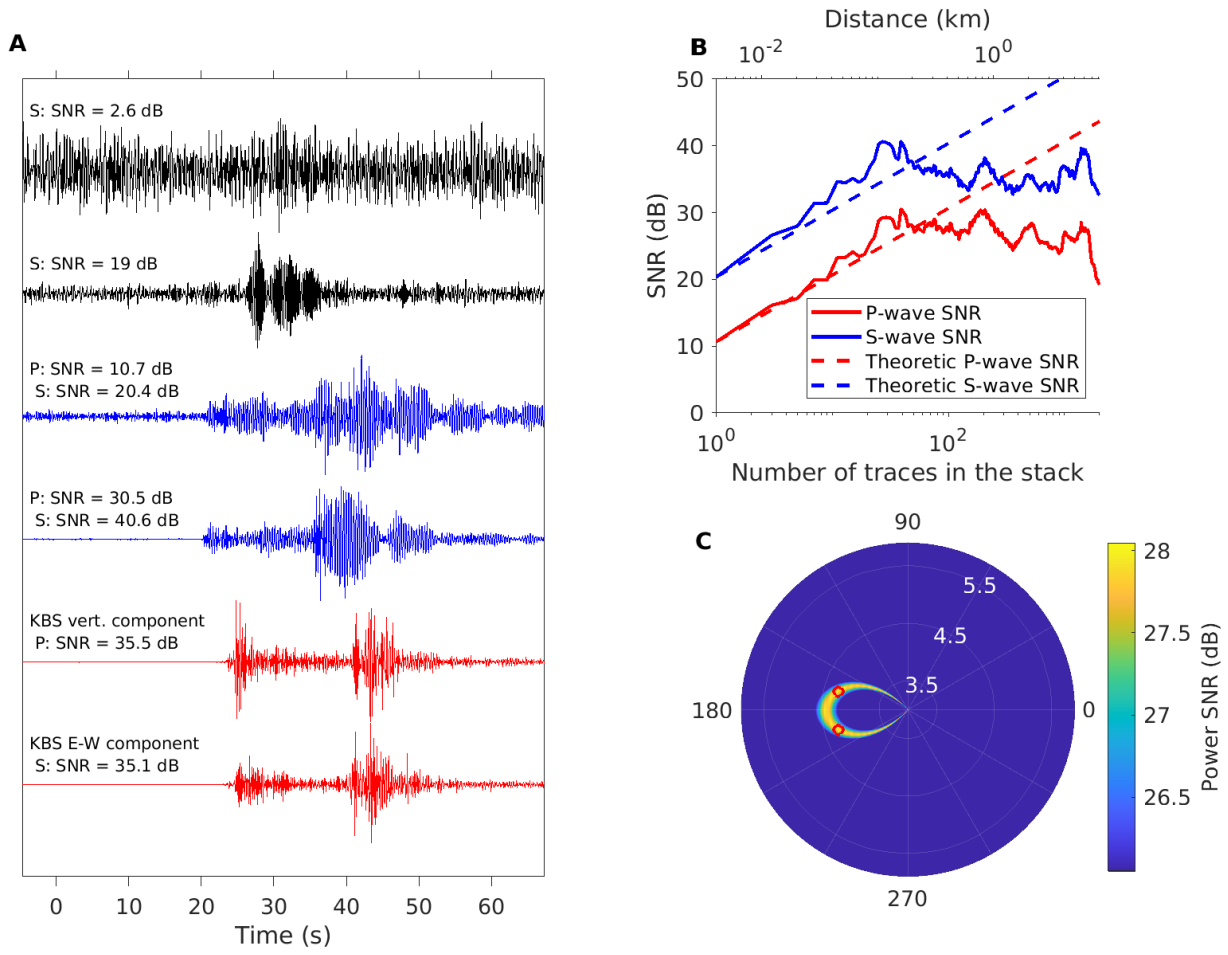

Fig. S2.

Increasing the SNR by finding the optimal apparent velocity and angle, and optimal number of traces in the stack that maintains signal coherence. (**A**) Comparison between single trace and a stack of 39 traces for channels at 114 km (black, high background noise level) and at 61 km (blue, low background noise level), against the vertical and west-east component of the KBS seismometer data (red). All traces are normalised relative to their absolute maximum. Stacking allows us to significantly improve the SNR and extract seismic signals otherwise buried in noise. The time-shift between the DAS and the KBS signal is caused by the difference in epicentral

distance (Figure 2). (**B**) SNR versus stacking length (in number of traces) for P- and S-waves around 61.3 km. Exceeding 39 traces reduces SNR. Dashed line corresponds to a $\sqrt{N}$ model for the improved SNR. (**C**) Beamforming for apparent P- and S-wave velocity and incidence angle using channels between 58.0-64.5 km with the same middle channels as the analysis in (**B**). The highest SNR values are found for angles of 193° and 192° relative to the cable axis, with velocities 4.25 and 2.45 km/s for P- and S-wave, respectively.

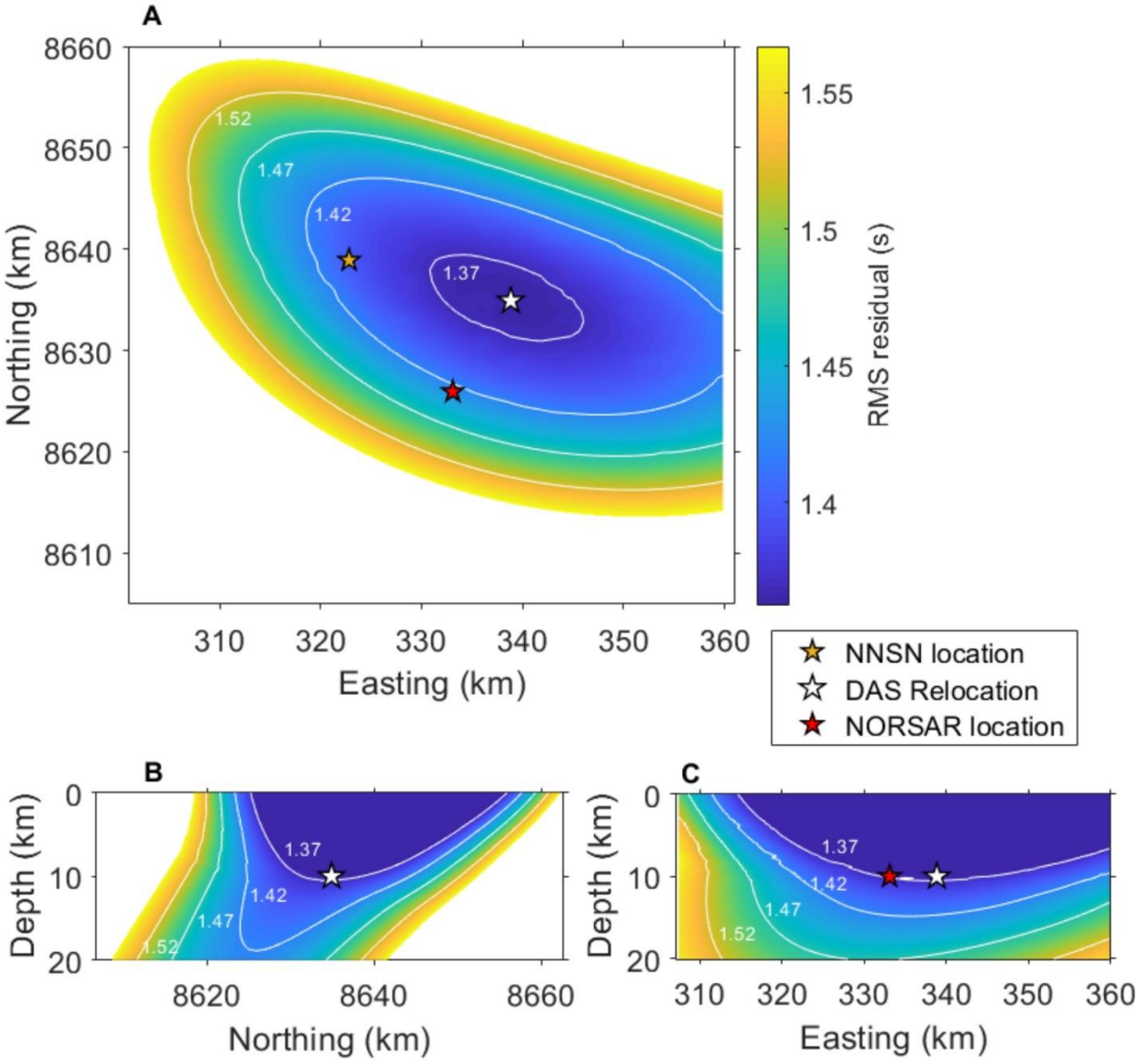

Fig. S3.

Localisation of the M_L 2.8 local earthquake using 53 DAS sensor points. The earthquake is relocated (white star) approximately 16.49 km south-east of the catalog location reported by NNSN (yellow star) and 10.65 km north-east of the NORSAR reported location (red star). The RMS of the relocated earthquake is 2.6% lower than the NNSN catalog location using ray tracing

to compute the eigenrays and 4.7% lower than the NORSAR catalog location. We used the dominant v_p/v_s = 1.65 ratio observed from the cable to estimate the S-wave travel time. (**A**) Shows the RMS values in the x-y plane for 10.0 km depth. (**B**) Shows the y-z plane through the DAS relocation. We observe a large uncertainty in depth towards the surface. (**C**) Shows the x-z plane through the DAS relocation, also showing the high depth uncertainty.

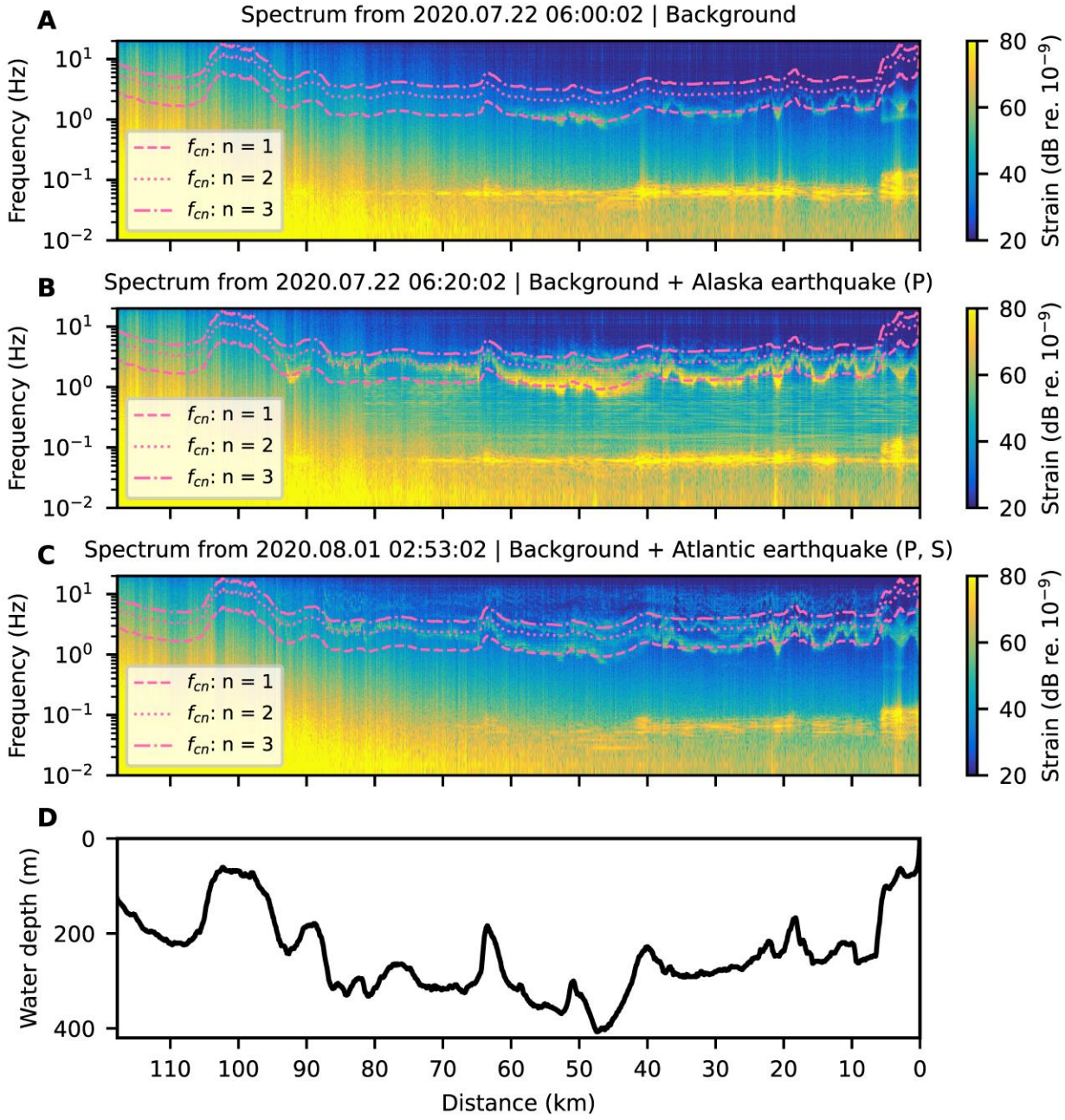

Fig. S4. Bathymetry and modal cut-off revealed by DAS.

Power spectral densities versus distance for (**A**) background microseismic noise, (**B**) during the arrival of the teleseismic P-wave signals from Alaska earthquake, and (**C**) during the Atlantic margin earthquake. (**D**) shows the water depth profile, which is correlated with the signals around

1–20 Hz. The plots are overlaid with the frequency functions defined by $f_{cn} = nc/(4H)$, where n is an integer, c = 1490 m/s is sound speed in water, and H is the water depth.

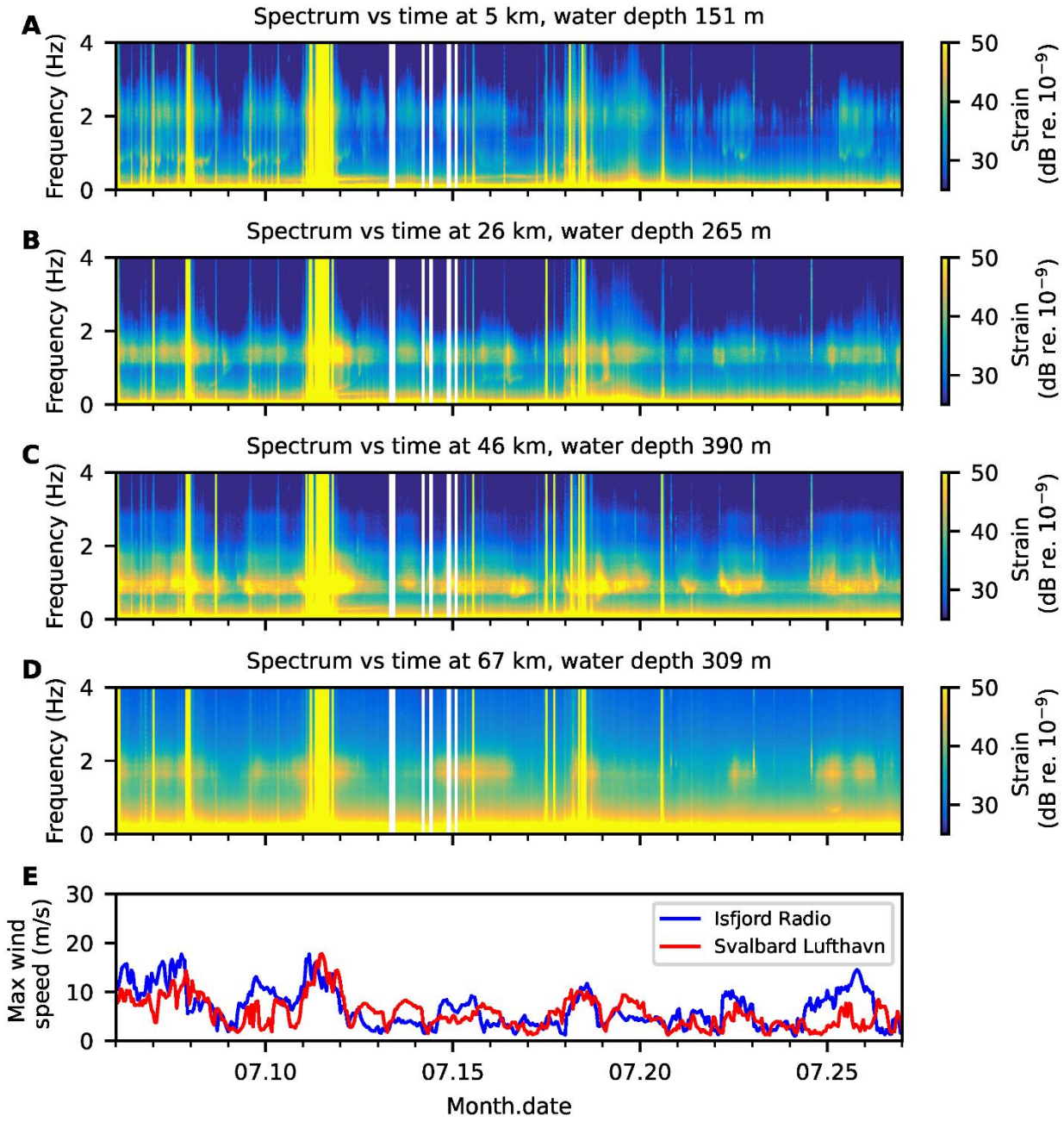

Fig. S5. Signal intensity correlated with local wind conditions.

Spectrograms (**A-D**) at 5, 26, 46, and 67 km along the cable. The vertical yellow bands show energy saturation associated with high local wind conditions (**E**). White vertical lines are break down in the data-stream.

Audio S1.

North Atlantic blue whale and fin whale vocalisations recorded on DAS cable on 2020.06.27. Blue whale arched sounds at 10 s and 75 s, possible D-calls at 30–70 s; possible fin whale vocalization at 40 s. Frequency scaled up by a factor of 3.5.

Audio S2.

Earthquake sound on 2020.08.01. Frequency scaled up by a factor of 20, from 125 Hz to 2500 Hz.